

Surface plasmon polaritons on soft-boundary graphene nanoribbons and their application as voltage controlled plasmonic switches and frequency demultiplexers

Ebrahim Forati and George W. Hanson*

*Department of Electrical Engineering and Computer Science, University of Wisconsin
Milwaukee, WI53211, USA*

E-mail: george@uwm.edu

Abstract

A graphene sheet gated with a ridged ground plane, creating a soft-boundary (SB) graphene nanoribbon, is considered. By adjusting the ridge parameters and bias voltage a channel can be created on the graphene which can guide TM surface plasmon polaritons (SPP). Two types of modes are found; fundamental and higher-order modes with no apparent cutoff frequency and with energy distributed over the created channel, and edge modes with energy concentrated at the soft-boundary edge. Dispersion curves, electric near-field patterns, and current distributions of these modes are determined. Since the location where energy is concentrated in the edge modes can be easily controlled electronically by the bias voltage and frequency, the edge-mode phenomena is used to propose a novel voltage controlled plasmonic switch and a plasmonic frequency demultiplexer.

*To whom correspondence should be addressed

Introduction

Graphene is the first two dimensional atomic crystal available to researchers, and has been the subject of intense study concerning both its fabrication and applications.^{1–13} Electrical properties of graphene, as represented by a local conductivity, are studied in many papers.^{14–23} It has been shown that the conductivity of graphene consists of interband and intraband contributions whose imaginary parts have different signs. Assuming an $e^{i\omega t}$ time convention, at lower frequencies and lower temperatures the intraband term with negative imaginary part dominates the conductivity, otherwise the conductivity has a positive imaginary part due to the interband contribution. Furthermore, it has been shown that a graphene sheet can support a single TM surface plasmon polariton, and only in the regime where the conductivity has negative imaginary part.^{16,24} Likewise, when conductivity has a positive imaginary part only a TE mode can propagate. However, TE modes are very loosely confined to the graphene surface and are not considered further here.

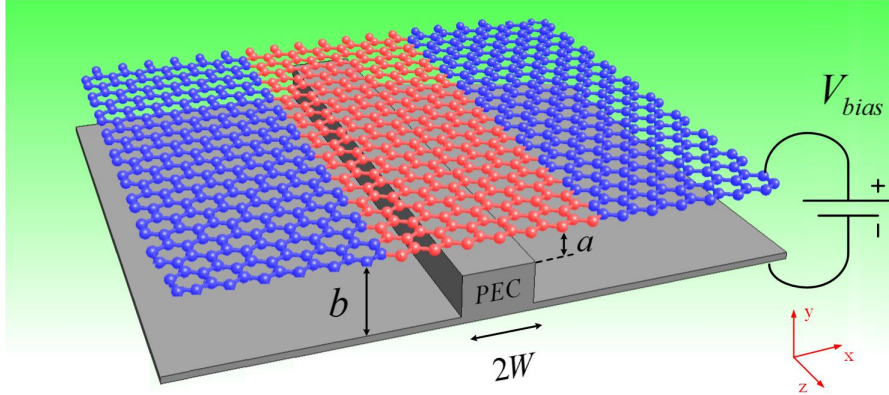


Figure 1: Graphene sheet gated with a ridged, perfect electrically-conducting (PEC) ground plane for the electrostatic bias, forming a soft-boundary graphene nanoribbon. The red area depicts the SPP channel having $\text{Im}(\sigma(x)) < 0$, and the blue area depicts the region where $\text{Im}(\sigma(x)) > 0$ and SPP propagation is prohibited.

The conductivity of graphene can be controlled by its carrier density, which can be varied by an electrostatic or magnetostatic bias, and/or chemical doping. This fact is used in²⁵ to implement a graphene based plasmonic switch. Recently, it has been proposed to use a perturbed ground plane as depicted in Fig. 1 in order to obtain different conductivities on the graphene, near and far from the ridge, by the use of a single bias voltage,²⁶ thereby creating a SPP propagation channel

parallel to the ridge. In²⁶ the ground plane ridge was assumed to form a conductivity profile with sharp features, i.e., to effectively form a hard-boundary (HB) graphene nanoribbon (GNR) wherein $\text{Im}(\sigma) < 0$ for $|x| < W$ and $\text{Im}(\sigma) > 0$ for $|x| > W$, where $2W$ is the ridge width and σ is assumed to be constant in each region. To remove the HB assumption, in²⁷ we studied the role of geometry and bias on forming the desired channel. In that work, rather than assuming a piece-wise constant conductivity, we determined the actual conductivity profile $\sigma(x)$ by finding the electrostatic charge distribution $\rho(x)$ on the graphene sheet from Laplace's equation, leading to the chemical potential $\mu_c(x)$ and the conductivity via the Kubo formula. It was shown that the ridged structure does indeed allow for the formation of a channel in the vicinity of the ridge for SPP propagation using a single bias, but that the resulting boundary has, as expected, a softened profile (i.e., a soft boundary (SB)) wherein the conductivity is not constant. The work²⁷ was concerned with the properties of the soft boundary and resulting channel, and the current distribution of the fundamental SPP mode. In this work we consider the various other modes that can propagate along the SB channel, including higher-order modes and edge modes. In particular, we show that unlike the HB case, for a soft boundary the higher-order modes have no apparent low-frequency/long-wavelength cutoff, although as frequency is lowered modal energy tends to spread out laterally along the effectively wider channel. We also show that low-loss edge modes can propagate for which the location where energy is concentrated can be controlled electronically. We then consider two applications of the structure, as a plasmonic voltage-controlled switch and a frequency demultiplexer.

Figure 2 shows the conductivity profile $\sigma(x)$ of the graphene sheet for a representative set of geometrical and electrical parameters; the SPP channel terminates where $\text{Im}(\sigma)$ becomes positive. The slope of the conductivity in the vicinity of the soft boundary can be adjusted by the ridge parameters, discussed in detail in.²⁷

Throughout this work, the parameters of Fig. 1 are set as $a = 25\text{nm}$, $b = 1\mu\text{m}$, $V_0 = 20\text{V}$, and $W = 25\text{nm}$. The mathematical formulations and numerical procedure are given in the supporting information.

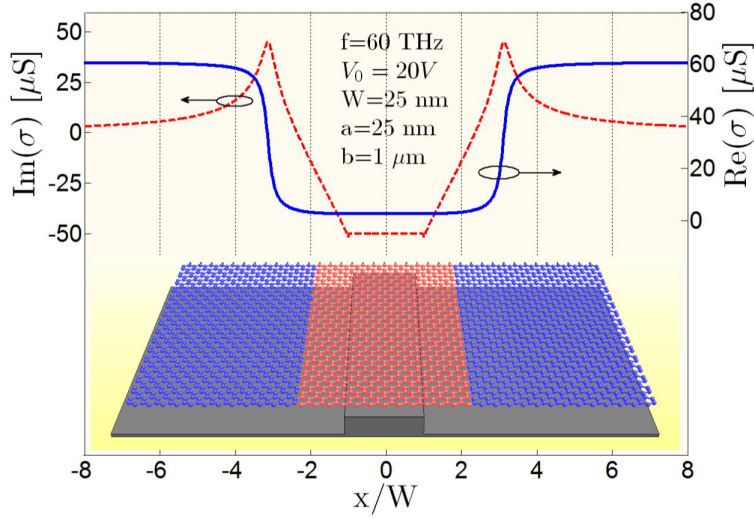


Figure 2: Conductivity distribution on the graphene sheet.

Soft boundary SPP modes

SPP modes for the geometry in Fig. 1 are calculated by a rigorous electromagnetic analysis based on an electric-field integral equation (see²⁷ and supporting information). Figure 3 shows the dispersion curves of the first three soft boundary modes. Also shown are the first four modes of a suspended¹ graphene nanoribbon with width 50nm and the same conductivity as for the SB modes for $|x| < W$, with $\sigma = 0$ for $|x| > W$. These modes are marked as hard boundary (HB) modes, and are the usual GNR modes. As discussed in several papers,^{28,29} for the HB GNR the first two modes (called edge modes since energy is concentrated at the graphene edge, similar to that found for a graphene half-space) asymptotically merge to the edge mode of a semi-infinite graphene sheet.^{29,30} The other higher order modes of the HB GNR become asymptotic to the single TM SPP mode²¹ that can propagate on an infinite graphene sheet. This HB behavior is shown in Fig. 3, where we also show that, unlike the HB case, for the soft boundary all modes become asymptotic to the infinite sheet SPP. In this regard, SB modes of the geometry are analogous to the sufficiently-higher-order modes (modes 3,4, ...) of the HB GNR.

¹We consider a suspended graphene nanoribbon rather than a nanoribbon over a ground plane since the modes are strongly confined to the graphene surface and do not interact with the ground plane (which merely serves to bias the graphene sheet).

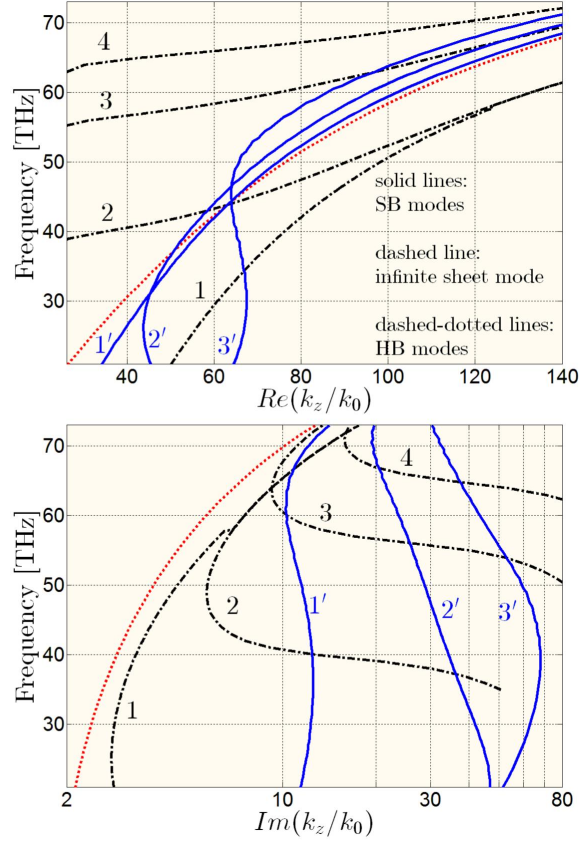


Figure 3: Modal dispersion curves for the SB case (blue). For convenience, the SPP for an infinite graphene sheet (at $\mu_c = 0.239$ eV) is also shown (red), as well as the modes of a HB GNR (black) with the same conductivity as the SB case for $|x| < W$ (and $\sigma = 0$ for $|x| > W$).

Figure 3 shows that there is no apparent cut off frequency for the SB modes. This is because, unlike a HB GNR with fixed width, as frequency decreases the effective width of the SB channel increases (i.e., the effect of the ridge perturbation which creates the propagation channel on the graphene sheet extends further away from the ridge as frequency is lowered). To clarify this, Fig. 4 shows the current, conductivity and field distribution of the first SB mode. Fig. 4(a) shows the normalized real part of the longitudinal current, $\text{Re}(J_z)$, and the imaginary part of the conductivity, $\text{Im}(\sigma)$, as a function of x . Since these are eigenmode currents, they are normalized so that $\|J_T\| = 1$, where J_T is the total current consisting of longitudinal and transverse components (i.e. $\int \left(|J_x(x)|^2 + |J_z(x)|^2 \right) dx = 1$). Fig. 4(b) shows the normalized magnitude of the longitudinal electric field $|E_z|$ in the transverse coordinate $(x - y)$. Here we define an effective width for the

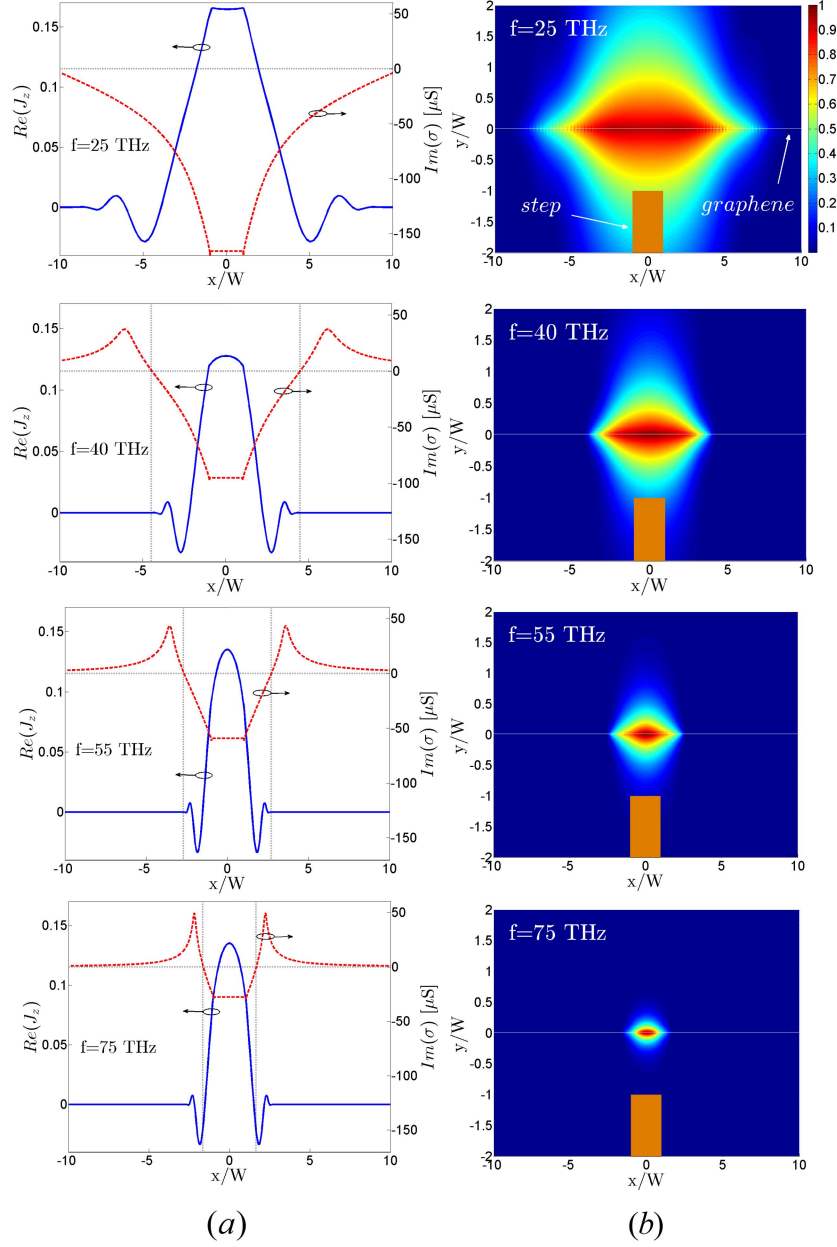


Figure 4: $\text{Re}(J_z(x))$ and $|E_z(x)|$ distributions of the first SB mode ($1'$ in Fig. 3) at four different frequencies. The conductivity profile ($\text{Im}(\sigma)$) is also shown.

channel (W_{eff}) as the width of the channel on the graphene sheet where $\text{Im}(\sigma(x)) < 0$, which occurs in the vicinity of the ridge (since only in this region can SPPs propagate). It is evident from Fig. 4 that W_{eff} increases as frequency decreases and therefore there is no cut off frequency for SB modes as exists for HB GNR modes (and, more generally, for all waveguides of fixed transverse dimensions), which is an important distinction between the SB and HB cases. Quantitatively,

W_{eff}/W is 21.13, 8.97, 5.4, and 3.3 at 25, 40, 55, and 75 THz, respectively.

The current distribution for SB modes is similar to those of HB GNR modes in the region $|x| < W$. Outside of this region the current vanishes after a few oscillations. These oscillations resemble the field distribution in the cladding of an optical fiber with graded index cladding.³¹ Since $\text{Im}(\sigma) > 0$ in the region $|x| > W_{\text{eff}}$, the current (and therefore the mode) is forced to be limited to the $|x| < W_{\text{eff}}$ region. However, this is not a necessary condition for mode confinement (although it is sufficient). In²⁷ we show that even when $\text{Im}(\sigma) < 0$ everywhere on the graphene sheet (e.g., at low frequency and higher temperature) it is still possible to have modes confined near the ridge. In fact, the confinement condition is that the conductivity boundaries are sharp enough so that the current concentrates in the vicinity of the ridge. As the boundaries become softer, by, say, lowering the ridge, the currents spread out further.

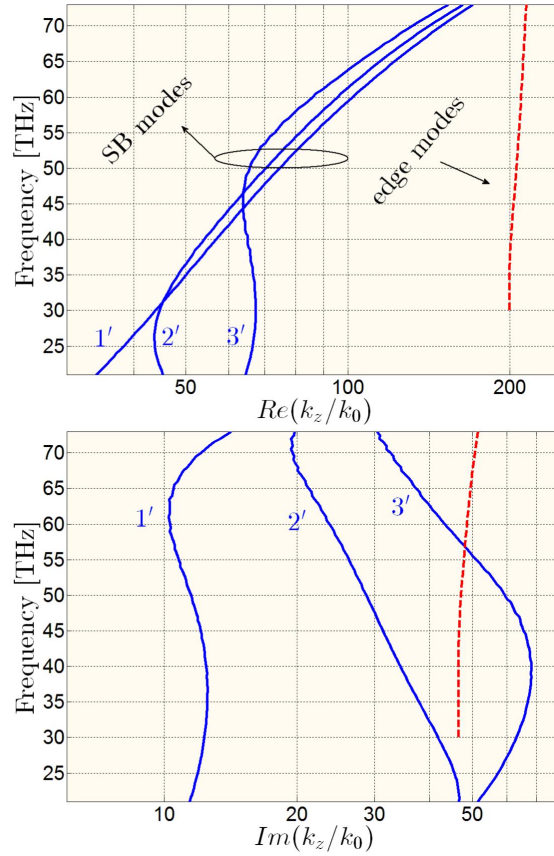


Figure 5: Dispersion curves of the geometry of Fig. 1 showing the previously-discussed bulk-like SB modes, and SB edge modes.

The current and field distributions for the second and third SB modes are provided in the supporting information. Further higher order SB modes are not as important since they are very lossy.

Soft boundary edge modes

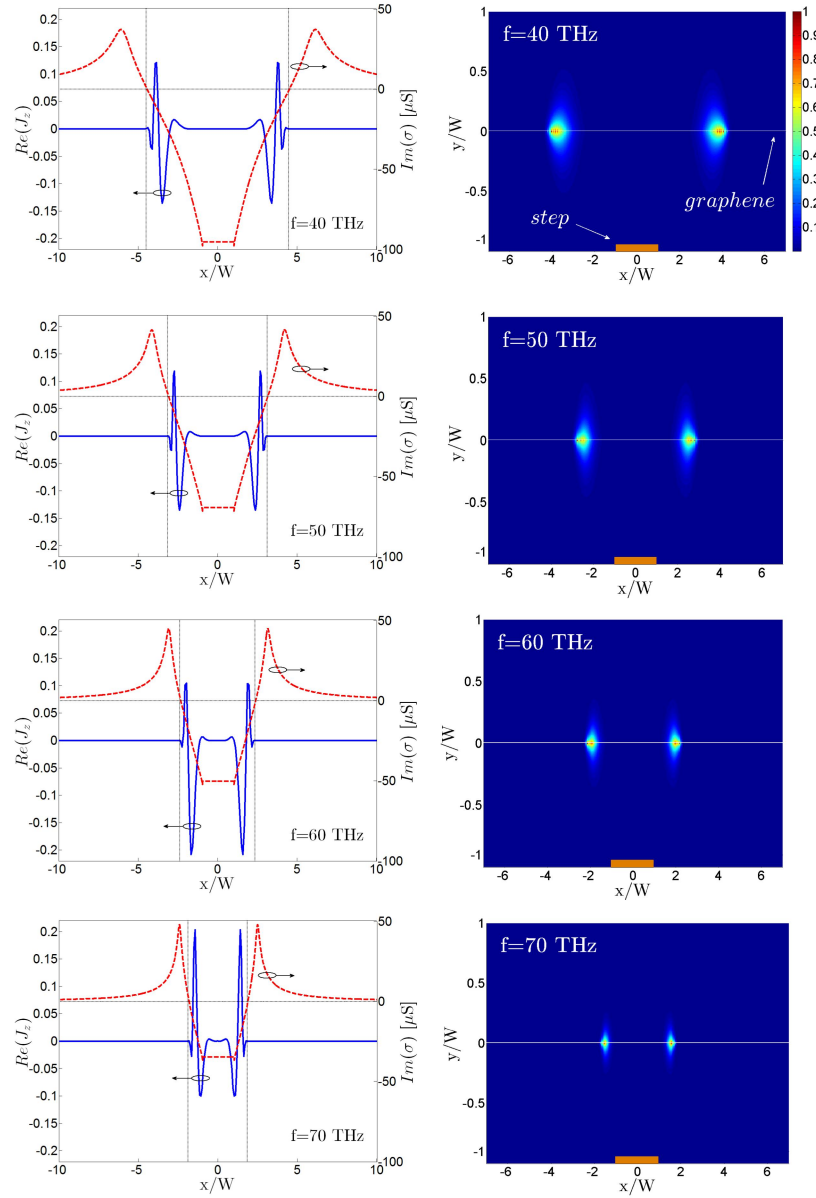


Figure 6: $\text{Re}(J_z(x))$ and $|E_z(x)|$ distributions of the even edge mode at four different frequencies.

As with a HB GNR, there are two degenerate edge modes for the geometry in Fig. 1, as considered in Fig. 5. These two even and odd edge modes propagate along edges of the created channel (i.e. in the region where $\text{Im}(\sigma)$ changes sign). As Fig. 5 shows, edge modes are slower and less dispersive than the previously-discussed SB bulk-like (since current spreads out over the bulk of the created channel) modes. Therefore, at lower frequencies where the boundary is softer, these modes become more important since they are much slower than other SB modes. Fig. 6 shows the current and field distributions of the even edge mode for four different frequencies. Obviously, the even and odd classification can be interchanged by the left and right edge modes as is done in some works.^{28,29} The SB edge modes have two important properties: First, they are fairly low-loss and slow, and therefore more tightly confined to the graphene surface than the bulk SB modes (which, nevertheless, are fairly tightly confined to the graphene surface). Second, their physical location relative to the ridge varies with the applied bias voltage and with frequency. The latter property makes the geometry useful for switching and demultiplexing applications, as proposed in the next section.

Plasmonic switch and demultiplexer

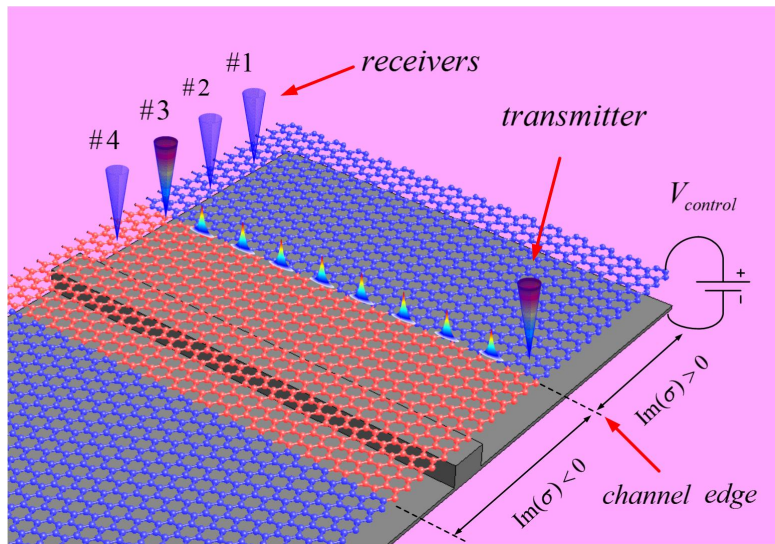


Figure 7: A scheme to form a voltage-controlled plasmonic switch/demultiplexer.

Since the effective width of the channel can be controlled by the bias voltage, the physical location where energy is concentrated for the edge modes can be easily controlled. One of the applications of this phenomena is a plasmonic voltage controlled switch as depicted in Fig. 7. By adjusting V_{control} in Fig. 7, the edge of the channel can be aligned with one of the receivers, and the edge mode can transfer energy from the transmitter to the desired receiver. In Fig. 7, the ridge parameters and bias voltage are assumed to form the channel such that it's edge is aligned with receiver 3.

On the other hand, it is evident from Fig. 6 that the channel width varies as frequency changes even with a fixed bias voltage. This suggests that we can design a plasmonic demultiplexer with the same geometry as shown in Fig. 7 with a fixed V_{control} . Then, e.g., lower frequencies can be transferred to receiver #1 and higher frequencies can be guided to, e.g., receiver #4. The characteristics of these plasmonic switches and demultiplexers can be determined by adjusting the distance between the receivers, ridge parameters, and the bias voltage range. Of course, it is assumed that the transmitter can excite a fairly wide area on the graphene sheet relative to the receivers, receivers, to allow the edge mode to be excited by a fixed-location transmitter.

Conclusion

Different SPP modes have been studied for the geometry depicted in Fig. 1, forming a soft boundary graphene nanoribbon. The dispersion curves, current, and field distributions were numerically calculated for a few bulk SB modes and for SB edge modes. It was shown that, unlike a hard boundary graphene nanoribbon, the bulk modes of the geometry do not have cut off frequencies due to the fact that the effective width of the channel increases as frequency decreases. It was also observed that the position of the edge modes varies according to the bias voltage and frequency. A novel voltage controlled plasmonic switch and plasmonic frequency multiplexer were proposed utilizing the SB edge modes, which propagate with low loss.

Supporting Information Available

The carrier density distribution of Fig. 1 (the graphene sheet is in the $y = 0$ plane and the center of the ridge is at $x = 0$) is²⁷

$$\frac{\rho(x)}{\epsilon_0 V_0} = \begin{cases} \frac{1}{a} & |x| < W \\ \frac{1}{b} + \sum_{n=1}^{\infty} \frac{n\pi}{b} C_n (-1)^n e^{-\frac{n\pi}{b}(|x|-W)} & |x| > W \end{cases} \quad (1)$$

where

$$C_n = -\frac{2b}{a} \left(\frac{1}{n\pi} \right)^2 \sin \left(n\pi \left(1 - \frac{a}{b} \right) \right). \quad (2)$$

In obtaining (2), a zeroth order approximation has been used to assume an x - independent potential in the region above the step ($|x| < W$). Otherwise, the problem needs to be solved numerically (e.g., by expanding the potentials as series for both $|x| < W$ and $|x| > W$ regions). The zeroth-order solution is a good approximation for $W \ll b$ and/or $a \ll b$ in Fig. 1.

This leads to the chemical potential

$$\mu_c(x) = \frac{\hbar}{e} v_F \sqrt{\frac{\pi \rho(x)}{e}} \quad (3)$$

where $v_F = 9.546 \times 10^5$ m/s is the Fermi velocity. The chemical potential is then used in the Kubo formula to find the graphene conductivity distribution $\sigma(x)$,³²

$$\begin{aligned} \sigma(x) = & \frac{je^2}{\pi \hbar^2 (\omega - j\Gamma)} \int_0^{\infty} \epsilon \left(\frac{\partial f_d(\epsilon, x)}{\partial \epsilon} - \frac{\partial f_d(-\epsilon, x)}{\partial \epsilon} \right) d\epsilon \\ & - \frac{je^2 (\omega - j\Gamma)}{\pi \hbar^2} \int_0^{\infty} \frac{f_d(-\epsilon, x) - f_d(\epsilon, x)}{(\omega - j\Gamma)^2 - 4(\epsilon/\hbar)^2} d\epsilon, \end{aligned} \quad (4)$$

where $-e$ is the charge of an electron, \hbar is the reduced Plank's constant, $f_d(\epsilon, x) = \left(\exp \left(\frac{\epsilon - \mu_c(x)}{k_B T} \right) + 1 \right)^{-1}$ is the Fermi-Dirac distribution, k_B is the Boltzmann's constant, and $\Gamma = 10^{13}$ 1/s is the phenomeno-

logical scattering rate.

The eigenmodes of the structure are found starting with Ohm's law

$$\mathbf{J}(x, \beta_z) = \boldsymbol{\sigma}(x) \mathbf{E}(x, b, \beta_z), \quad (5)$$

where the Fourier transform pair is defined as

$$\mathbf{E}(x, y, \beta_z) = \int_{-\infty}^{\infty} \mathbf{E}(x, y, z) e^{-j\beta_z z} dz \quad (6)$$

$$\mathbf{E}(x, y, z) = \frac{1}{2\pi} \int_{-\infty}^{\infty} \mathbf{E}(x, y, \beta_z) e^{j\beta_z z} d\beta_z. \quad (7)$$

Current and electric field are related as

$$\mathbf{E}(x, y, \beta_z) = (k_0^2 + \nabla_{\beta_z} \nabla_{\beta_z} \cdot) \quad (8)$$

$$\int_{x'} g(x, y, x', \beta_z) \frac{\mathbf{J}(x', \beta_z)}{j\omega\epsilon_0} dx'$$

where $\nabla_{\beta_z} = \frac{d}{dx} \hat{\mathbf{x}} + \frac{d}{dy} \hat{\mathbf{y}} + j\beta_z \hat{\mathbf{x}}$ and the Green's function is

$$g(x, y, x', \beta_z) = \frac{1}{2\pi} K_0 \left(\sqrt{\beta_z^2 - k_0^2} \sqrt{(x - x')^2 + (y - b)^2} \right), \quad (9)$$

$K_0(x)$ being the zero order modified Bessel function of the first kind.

Equations (5) and (8) form an integral equation whose null space gives the eigenmodes of the structure (i.e., different β_z and their associated currents). The pulse function collocation method is used to solve the integral equation, with point matching at the center of the pulses. The eigen-currents in Figs. 4 and 6 are normalized so that the 2-norm of the eigen current vector (consists of transverse and longitudinal components) is unity ($\int (|J_x(x)|^2 + |J_z(x)|^2) dx = 1$.)

After finding the currents associated with the modes, (8) is used to find the field distributions

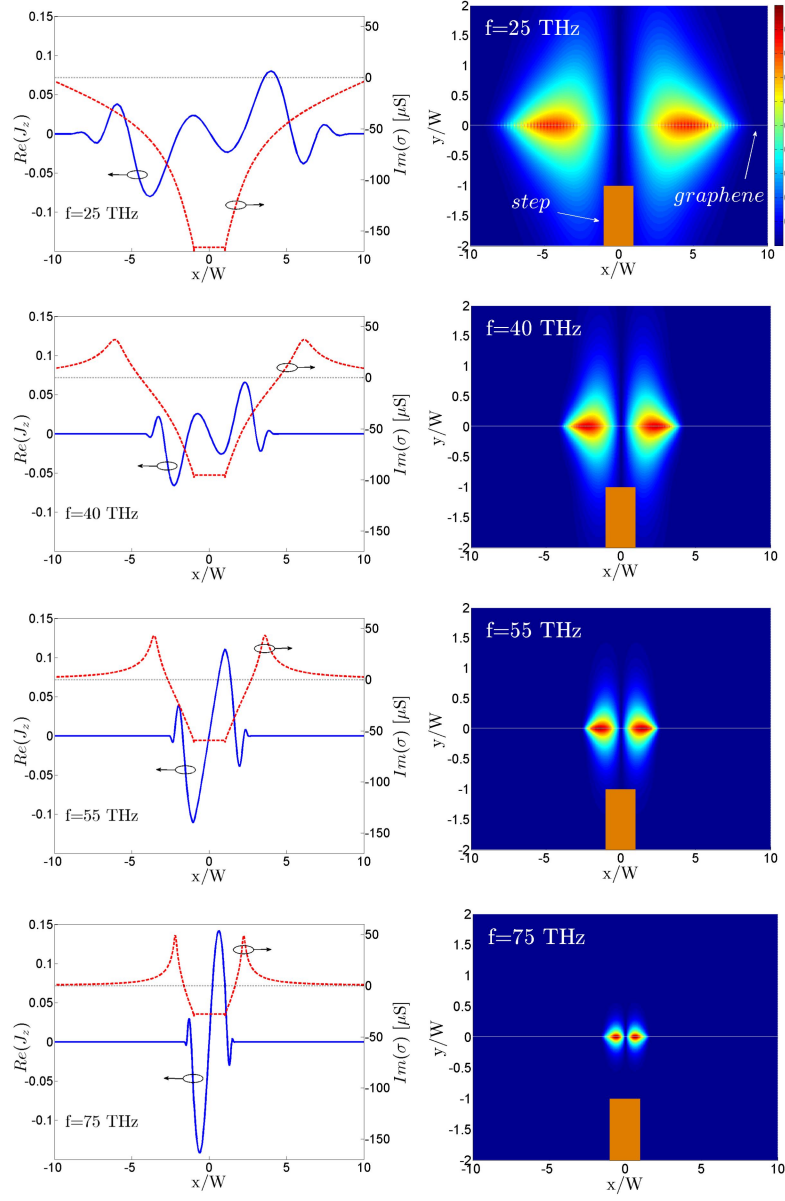


Figure 8: $\text{Re}(J_z(x))$ and $|E_z(x)|$ distributions of the second SB mode (2' in Fig. 3) at four different frequencies.

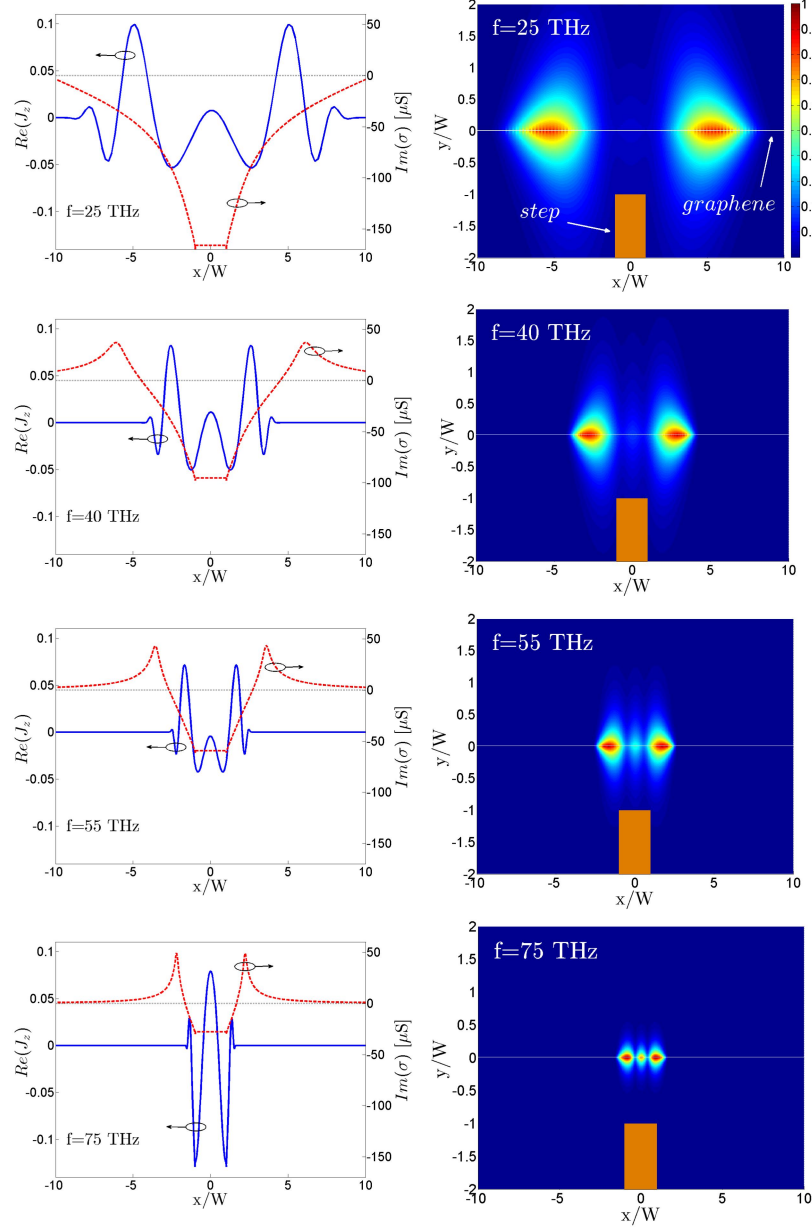


Figure 9: $Re(J_z(x))$ and $|E_z(x)|$ distributions of the third SB mode (3' in Fig. 3) at four different frequencies.

$$E_x(x, y) = \frac{k_0^2}{2\pi j\omega\epsilon_0} \int_{x'} K_0(\alpha) J_x(x') dx' + \frac{1}{2\pi j\omega\epsilon_0} \int_{x'} \left\{ \frac{\partial^2}{\partial x^2} [K_0(\alpha)] J_x(x') + j\beta \frac{\partial}{\partial x} [K_0(\alpha)] J_z(x') \right\} dx' \quad (10)$$

$$E_y(x, y) = \frac{1}{2\pi j\omega\epsilon_0} \frac{\partial}{\partial y} \int_{x'} \left\{ \frac{\partial}{\partial x} [K_0(\alpha)] J_x(x') + j\beta K_0(\alpha) J_z(x') \right\} dx' \quad (11)$$

$$E_z(x, y) = \frac{k_0^2}{2\pi j\omega\epsilon_0} \int_{x'} K_0(\alpha) J_z(x') dx' + \frac{1}{2\pi j\omega\epsilon_0} \int_{x'} \left\{ j\beta \frac{\partial}{\partial x} [K_0(\alpha)] J_x(x') - \beta^2 K_0(\alpha) J_z(x') \right\} dx' \quad (12)$$

in which

$$\alpha = \sqrt{q_z^2 - k^2} \sqrt{(x - x')^2 + (y - b)^2}. \quad (13)$$

The currents ($\text{Re}(J_z(x))$) and field distributions ($|E_z^2(x, y)|$) associated with the second and third SB modes (2' and 3' in Fig. 6) at different frequencies are given in Figs. 8 and 9, respectively.

Two assumptions are made in the calculation of the surface modes. The conductivity distribution based on the electrostatic charge distribution is assumed to be only slightly perturbed by the modal fields, i.e., $\frac{\nabla \cdot \mathbf{J}}{j\omega} \ll \rho$ where ρ is the static charge density and \mathbf{J} is the modal current density. The second assumption is that the the ground plane (and its ridge) are far enough from the surface that the ground plane does not interact with the (tightly-confined) modal fields. The parameters of the geometry were chosen so that these assumptions are both valid.

References

- (1) Novoselov, K. S.; Geim, A. K.; Morozov, S. V.; Jiang, Y., D. and Zhang; Dubonos, S. V.; Grigorieva, I. V.; Firsov, A. A. *Science* **2004**, *306*, 666–669.
- (2) Zhang, Y.; Tan, Y. W.; Stormer, H. L.; Kim, P. *Nature* **2005**, *438*, 201–204.

- (3) Berger, C.; Song, Z.; Li, X.; Wu, X.; Brown, N.; Naud, C.; Mayou, D.; Li, T.; Hass, J.; Marchenkov, A. N. *Science* **2006**, *312*, 1191–1196.
- (4) Geim, A. K.; Novoselov, K. S. *Nat. Mater.* **2007**, *6*, 183–191.
- (5) Nair, R. R.; Blake, P.; Grigorenko, A. N.; Novoselov, K. S.; Booth, T. J.; Stauber, T.; Peres, N. M. R.; Geim, A. K. *Science* **2008**, *320*, 1308.
- (6) Bonaccorso, F.; Sun, Z.; Hasan, T.; Ferrari, A. C. *Nat. Photon* **2010**, *4*, 611–622.
- (7) Schedin, F.; Lidorikis, E.; Lombardo, A.; Kravets, V. G.; Geim, A. K.; Grigorenko, A. N.; Novoselov, K. S.; Ferrari, A. C. *ACS Nano* **2010**, *4*, 5617–5626.
- (8) Geim, A. K. *Science* **2009**, *324*, 1530–1534.
- (9) Mak, K. F.; Sfeir, M. Y.; Wu, Y.; Lui, C. H.; Misewich, J. A.; Heinz, T. F. *Phys. Rev. Lett.* **2008**, *101*, 196405.
- (10) Mueller, T.; Xia, F.; Freitag, M.; Tsang, J.; Avouris, P. *Phys. Rev. B* **2009**, *79*, 245430.
- (11) Xia, F. N.; Mueller, T.; Lin, Y. M.; Valdes-Garcia, A.; Avouris, P. *Nat. Nanotechnol.* **2009**, *4*, 839–843.
- (12) Lee, E. J. H.; Balasubramanian, K.; Weitz, R. T.; Burghard, M.; Kern, K. *Nat. Nanotechnol.* **2008**, *3*, 486–490.
- (13) Castro Neto, A. H.; Guinea, F.; Peres, N. M. R.; Novoselov, K. S.; Geim, A. K. *Rev. Mod. Phys.* **2009**, *81*, 109–162.
- (14) Falkovsky, L. A.; Varlamov, A. A. *Eur. Phys. J. B* **2007**, *56*, 281–284.
- (15) Falkovsky, L. A.; Pershoguba, S. S. *Phys. Rev. B* **2007**, *76*, 153410.
- (16) Mikhailov, S. A.; Ziegler, K. *Phys. Rev. Lett.* **2007**, *99*, 016803.
- (17) Gusynin, V. P.; Sharapov, S. G.; Carbotte, J. P. *Phys. Rev. Lett.* **2006**, *96*, 256802.

- (18) Gusynin, V. P.; Sharapov, S. G. *Phys. Rev. B* **2006**, *73*, 245411.
- (19) Peres, N. M. R.; Neto, A. C.; Guinea, F. *Phys. Rev. B* **2006**, *73*, 195411.
- (20) Hanson, G. W. *IEEE Trans. Antennas Propagat.* **2008**, *56*, 747–757.
- (21) Hanson, G. W. *J. Appl. Phys.* **2008**, *103*, 064302.
- (22) Peres, N. M. R.; Guinea, F.; Neto, A. C. *Phys. Rev. B* **2006**, *73*, 125411.
- (23) Ziegler, K. *Phys. Rev. B* **2007**, *75*, 233407.
- (24) Hanson, G. W.; Forati, E.; Linz, W.; Yakovlev, A. *Phys. Rev. B* **2012**, *86*, 235440 (1–9).
- (25) Gómez-Díaz, J. S.; Perruisseau-Carrier, J. *Optics Express* **2013**, *21*, 15490–15504.
- (26) Vakil, A.; Engheta, N. *Science* **2011**, *332*.6035, 1291–1294.
- (27) Forati, E.; Hanson, G. W. *Journal of optics* **In review**,
- (28) Nikitin, A. Y.; Guinea, F.; Garcia-Vidal, F. J.; Martin-Moreno, L. *arXiv* **2011**, *1107.5787*.
- (29) Sounas, D. L.; Caloz, C. *Appl. Phys. Lett.* **2011**, *98*, 021911.
- (30) Wang, W.; Apell, P.; Kinaret., J. *Phys. Rev. B* **2011**, *84*.8, 085423.
- (31) Kong, M.; Shi., B. *Fiber and integrated optics* **2006**, *25*, 305–321.
- (32) Gusynin, V. P.; Sharapov, S. G.; Carbotte, J. P. *J. Phys.: Condens. Matter* **2007**, *19*.2, 026222.

This material is available free of charge via the Internet at <http://pubs.acs.org/>.